ISSN 1024-8560, Atmospheric and Oceanic Optics, 2019, Vol. 32, No. 6, pp. 628–642. © Pleiades Publishing, Ltd., 2019.
Russian Text © The Author(s), 2019, published in Optika Atmosfery i Okeana.

REMOTE SENSING OF ATMOSPHERE, HYDROSPHERE, AND UNDERLYING SURFACE

Simultaneous Reconstruction of the Complex Refractive Index and the Particle Size Distribution Function from Lidar Measurements: Testing the Developed Algorithms

S. V. Samoilova*

V.E. Zuev Institute of Atmospheric Optics, Siberian Branch, Russian Academy of Sciences, Tomsk, 634055 Russia
**e-mail: ssv@seversk.tomsknet.ru*

Received January 24, 2019; revised January 24, 2019; accepted May 31, 2019

Abstract—A method for the joint determination of microphysical aerosol characteristics, namely, the complex refractive index $m = m_{\text{real}} + im_{\text{image}}$ and spherical-particle size distribution function $U(r)$, from the data of nighttime lidar sensing at wavelengths of 355–1064 nm is proposed. During their simultaneous estimations, it is useful to directly minimize the discrepancy functional $\Phi(m)$ in the range of the physically justified m. The principal limitations due to a wider region of the global minima of $\Phi(m)$ appear at $m_{\text{image}}^{\text{true}} \in [0.01, 0.04]$ and give rise to a potential shift of the resulting values of $m_{\text{real}}^{\text{est}}$ and $m_{\text{image}}^{\text{est}}$. A simultaneous use of several functionals gives a better estimate of m due to different sets of the respective optical characteristics. The problem in retrieving the size distribution function is caused by the information content of the coarse particle measurements. The statistical regularization method offers an unambiguous estimation of $U(r)$ for the mean radius up to 3 μm and gives an admissible estimate for larger radii. The algorithms are tested on eight values of absorption, when one value corresponding to one $m_{\text{image}}^{\text{true}}$ is associated with 50 empirical models of the distribution function.

Keywords: aerosol, lidar, particle size distribution function, complex refractive index
DOI: 10.1134/S1024856019060137

INTRODUCTION

Studying peculiarities of changes in the atmospheric aerosol is a significant part of investigating the complex of physical and chemical processes forming the Earth's climate. Different techniques for the determination of the aerosol composition, as well as shapes and dimensions of aerosol particles, were developed. Satellite systems make it possible to carry out the global monitoring of aerosol: MODIS [1], POLDER/PARASOL [2], and CALIOP [3]. Observations with the use of ground-based instruments provide a more detailed and exact information about aerosol characteristics at specific geographical points. Study of the horizontal distribution of the aerosol microphysical characteristics—the complex refractive index (CRI or $m = m_{\text{real}} + im_{\text{image}}$) and the particle size distribution function (SDF or $U(r)$)—has become possible since the development of the monitoring networks for the atmosphere, in particular AERONET (Aerosol Robotic Network) [4], and the methods for interpreting the observational data [5, 6]. Regional lidar networks—EARLINET [7], ADNET [8], and CIS-LiNet [9]—and the global GALION network [10] are intended to complement passive measurements with active ones, first of all by those giving information about the vertical aerosol distribution in the troposphere.

Since March 2006, measurements in Tomsk (56° N, 85° E) have been carried out within the framework of the CIS-LiNet project [9]. In daytime, the system records signals caused by elastic scattering at three wavelengths λ_{0i} = 355, 532 (polarization measurements), and 1064 nm. At night, there is an additional option of detecting the Raman scattering for two shifted wavelengths in the ultraviolet and visible ranges, λ_{Ri} = 387 and 607 nm. Such data collection allows one to estimate three backscattering coefficients $\beta(\lambda_{0i}, z)$ at λ_{0i} = 355, 532, and 1064 nm and two extinction coefficients $\sigma(\lambda_{0i}, z)$ at λ_{0i} = 355 and 532 nm. The $(3\beta + 2\sigma)$ system is accepted as standard for the GALION world network [10]. In the nearest future, it is planned to launch a similar system into the space [11].

Errors in determination of the optical coefficients for lidar systems of $(3\beta + 2\sigma)$ type are maximal in the UV region and amount to ~20% (σ) and ~10% (β) in the boundary layer of the atmosphere [12]. A well-posed numerical differentiation algorithm we used allows them to be decreased to ~10% (σ) and ~5% (β), including for the free troposphere [13]. The spectral

set of the optical coefficients and the errors in their estimation allow us to proceed to reconstruction of the vertical distribution of the microphysical aerosol characteristics.

Specialists in the field of solving inverse problems of aerosol light scattering began to study possibilities of retrieving the aerosol microstructure many years ago [14–18]; the variety of the main directions of study and results were presented in [19–24]. In particular, parameters of the bimodal SDF are correctly estimated for the geometric mean radius of fine R_{fine} and coarse R_{coarse} particles within the range of $0.1 \le R_i \le 6$ μm in AERONET measurements; for more details, see [24].

From the mathematical point of view, the optical coefficients of the aerosol layer located at a distance z from the lidar are connected with microphysical characteristics by the system of linear integral equations

$$\int_{r_{\min}}^{r_{\max}} K_j(m,r,z)U(r,z)dr + \varepsilon_j^{\text{meas}}(z) = g_j^{\text{meas}}(z), \quad (1)$$
$$j = \{\beta(355),\beta(532),\beta(1064),\sigma(355),\sigma(532)\} = 1,\ldots,5,$$

where $g_j^{\text{meas}}(z)$ specify the set of measured optical coefficients for the corresponding wavelength, $\varepsilon_j^{\text{meas}}(z)$ are the measurement errors, $U(r, z)$ is the volume, bimodal particle size distribution function, and $K_j(m, r, z)$ are the equation kernels depending on the refractive index and particle shape. The variable z, not relevant in the description of the methods, is omitted below to simplify the formulas. In lidar sensing, first investigations of inversion methods for (1) were based on the Mie theory [25]; aerosol was modeled as a polydisperse system of homogeneous spherical particles [26–32]. In [33–40], features of CRI + SDF were considered for different types of aerosol, in particular, for spheroids according to [41–43].

Theoretical aspects of determining microphysical characteristics of aerosol by sensing data were considered in [28, 30, 31, 37, 38, 44–46]. The analysis demonstrates the presence of two serious problems in determining them: (i) a biased retrieval of the distribution function for the coarse fraction even in the cases of a known refractive index; (ii) an uncertainty in reconstructing m even for a known $U(r)$. The SDF is linearly connected with optical coefficients; if the CRI is known (or preliminarily estimated), its retrieval is reduced to inversion of a system of linear algebraic equations. The problem for coarse particles stems from the information content of the measurements at $r > 1$ μm, and the biased estimates of $U_{\text{coarse}}(r)$ are predetermined by the a priori choice of the stabilizer order [28, 30, 44].

A reconstruction of the refractive index is a more complicated problem in view of the absence of certain commonly accepted methods working equally well for any set of the measured characteristics. In the general form, estimating the CRI is reduced to direct minimization of the discrepancy functional $\Phi(m)$ over all physically justified values of the m components. The functional shows the difference between optical coefficients *measured* and *calculated* from the reconstructed microphysical characteristics according to (1). If there are no errors (experimental or mathematical, related to special features of estimating $U(r)$), for any index value there would be a single minimum $\Phi(m) \equiv 0$ [45]. The presence of noises distorts the functional's surface and a false minimum could become the global one. The differences in the CRI lead to incorrect calculations of kernels of (1) and to the deformation of the SDF ([38, Table 2] or [46, Fig. 4]). For a polarization nephelometer, a serious investigation of possibilities for estimating $m + U(r)$ was presented in [47, 48].

An alternative for the developed algorithms of interpreting nighttime lidar measurements are GARRLiC (Generalized Aerosol Retrieval from Radiometer and Lidar Combined data) [49] and a simplified version LiRIC (Lidar/Radiometer Inversion Code) [50] (an automated package was created). The algorithms are based on the joint use of AERONET and EARLINET (only 3β) data during daylight hours. A combined use of the lidar and photometric measurements is an advantage in the case of 'dust' or 'volcanic' aerosol characterized by a larger contribution from the coarse fraction. For the 'urban pollution' and 'biomass burning' models with the dominant contribution of the fine fraction, there is no qualitative improvement of either CRI part. Nighttime measurements allow one to determine vertical profiles of CRI + SDF with the optical thickness of the tropospheric aerosol ≤ 0.1 at a wavelength of 532 nm; for more details, see [46, Section 5 and Fig. 5].

In this work, the optical coefficients are calculated by values of the sought quantities $m^{\text{true}} + U^{\text{true}}(r)$ according to (1); random noise is imposed on the resulting $(3\beta + 2\sigma)$ values, which is evenly distributed in the range of $-5\% \le \varepsilon_j^{\text{meas}} \le 5\%$ for every coefficient g_j^{meas} (the direct problem). Then, a reconstruction of $m^{\text{est}} + U^{\text{est}}(r)$ is performed, taking into consideration special features of estimating these two characteristics (the inverse problem). For both problems, the following approximations are used: (i) spherical particles, (ii) spectrum-averaged refractive index, and (iii) CRI value common for different SDF fractions. In Section 1, the method for retrieving the distribution function at a known refractive index is justified. In Subsection 1.2, features of the chosen method of statistical regularization are described. The advantages of its use are presented completely in [44]. Sections 2 and 3 give a detailed description of the algorithm for simultaneous determination of two microphysical characteristics. Subsections 2.1 and 2.2 show the variations in the CRI errors with increasing absorption and indicate the region of its maximum errors for a lidar system. Section 3 illustrates possibilities of a correct determination of CRI + SDF.

1. RETRIEVAL OF THE SIZE DISTRIBUTION FUNCTION

For a given (or already found) CRI, an expansion is performed of the sought-for distribution function with respect to the known system of basis functions $B_k(r)$ with unknown weighting coefficients u_k:

$$U(r) = \sum_k B_k(r)u_k + \varepsilon^{\text{base}}(r). \quad (2)$$

According to [26–29], a set of triangular basis functions with floating boundaries $r_{\min}$, $r_{\max}$ is used. The specific form of $B_k(r)$ slightly affects the quality with which the distribution function is retrieved and their number can vary [28]. Taking into account expansion (2), system of integral equations (1) is reduced to the system of equations for the vector of the weighting coefficients $\mathbf{u} = \mathbf{u}_{\text{fine}} + \mathbf{u}_{\text{coarse}}$:

$$\mathbf{Au} + \boldsymbol{\varepsilon} = \mathbf{g}, \quad (3)$$

where $\varepsilon_j = \varepsilon_j^{\text{meas}} + \varepsilon_j^{\text{math}}$ is the sum of experimental and mathematical errors, $\varepsilon_j^{\text{math}} = \int K_j(m,r)\varepsilon^{\text{base}}(r)dr$, and the components of the matrix $\mathbf{A}$ are written in the form $A_{jk}(m) = \int K_j(m,r)B_k(r)dr$. To invert Eq. (1), it is expedient to use in the first approximation a logarithmic scale of radii r_k. This allows results of estimation for fine and coarse particles to be considered in one scale. If we set the single value of $r_{\min} = 0.04$ μm and 6 values of $r_{\max} = 7.5–10$ μm (with a step of 0.5 μm), the average values over the abscissa $U(r)$ are as follows: $r_{\text{fine},\,k} = 0.067$, 0.10, 0.16, 0.24, 0.36, and 0.56 for $k =$ 1–6 and fine mode; $r_{\text{coarse},\,k} = 0.72$, 1.08, 1.62, 2.42, 3.36, and 5.42 for $k = 7–12$ and coarse mode. Moreover, inversion of (3) provides positive definiteness of the sought-for expansion coefficients u_k [13], which is a necessary condition for estimating the refractive index [5].

In the first series of numerical experiments, errors in estimating the SDF at a known CRI are studied. The SDF models are the solutions obtained at the Zvenigorod AERONET website (http://aeronet.gsfc.nasa.gov) in 2011–2012 (totally, 462 empirical models). The models are associated with one of four values $m_{\text{real}}^{\text{true}} = 1.5$, 1.55, 1.6, and 1.65; the imaginary part does not vary, $m_{\text{image}}^{\text{true}} \equiv 0$.

1.1. Tikhonov's Regularization Method

A solution of Eq. (3), robust against the measurement errors g_j and based on the Tikhonov regularization method [51], can be written in an explicit form [52]:

$$\mathbf{u} = (\mathbf{A}^{\text{T}}\mathbf{A} + \alpha\mathbf{Q})^{-1}\mathbf{A}^{\text{T}}\mathbf{g}, \quad (4)$$

where T denotes the transposition operation, α is the regularization parameter, and $\mathbf{Q}$ is a square matrix. The quadratic form $u^{\text{T}}\mathbf{Q}u$ is (to within a constant) is a finite difference approximation of the Tikhonov stabilizer

$$\Omega[u] = \int \left\{ q_0 u^2 + q_1 \left[\frac{du}{dr}\right]^2 + q_2 \left[\frac{d^2u}{dr^2}\right]^2 + \ldots \right\} dr,$$

where q_i are given nonnegative quantities. In particular, if $q_0 \neq 0$ (other $q_i = 0$), regularization of zero order $\mathbf{Q} \equiv \mathbf{Q}_0 = \mathbf{I}$ (the unit matrix) is used. At $q_0 \neq 0$ and $q_1 \neq 0$, one can obtain from (4) a solution with the first order stabilizer; the matrix $\mathbf{Q} = q_1\mathbf{D}_1\mathbf{D}_1^{\text{T}} + q_0\mathbf{I}$ has the banded form with a nonzero main diagonal and two nonzero diagonals adjacent to it. Similarly, one can also obtain the matrices for higher order derivatives. In the problem under consideration, basis functions in (2) are chosen to provide a uniform expansion of $U(r)$ on the ln r axis. It is necessary to take into account that elements of the matrix $\mathbf{Q}$ in (4) depend on r. Otherwise, the value of α can be overestimated in the region of small values of the radius (which leads to smoothing of $U_{\text{fine}}(r)$) and/or underestimated in the region of large values (with possible oscillations of $U_{\text{coarse}}(r)$).

Results of solving by Tikhonov's regularization method are presented in Fig. 1. The volume SDF was retrieved for stabilizers of the zero (TM0), first (TM1), and second (TM2) orders providing smoothness of the function itself and its derivatives. In the top panel of the figure, resolving possibilities of (4) are shown on an example of estimating the volume concentration of fine $V_{\text{fine}} = \int U_{\text{fine}}(r)dr$ ($0.04 < r < 0.6$ μm, the left panel of Fig. 1) and coarse $V_{\text{coarse}} = \int U_{\text{coarse}}(r)dr$ ($0.6 < r < 10$ μm, the right panel) particles; the calculations involved retrieved $U^{\text{est}}(r)$, using a total of 462 models. Each column of histograms indicates the number of realizations (in percent of 462) in which the error in estimating the parameter was within the indicated limits. Since the accuracy of retrieving the fine aerosol mode is much higher, the step sizes for the histograms are set as 1% and 5% for V_{fine} and V_{coarse}, respectively. The bottom part of the figure illustrates the change in 2 of 462 profiles of $U^{\text{est}}(r)$ obtained according to (4) and (2).

Analysis of the results demonstrates that, first, U_{fine} is retrieved with a better quality using the logarithmic derivative; the stabilizer order slightly affects the determination errors [44, Fig. 1]. Second, the accuracy of estimating U_{coarse}, on the contrary, is caused by the stabilizer choice. For all retrieved $U_{\text{coarse}}^{\text{est}}(r)$, the following quantities manifest themselves: (i) $R_{\text{coarse}}^{\text{est}} <$ 2.5 μm for the zero order regularization ($\mathbf{Q} = \mathbf{Q}_0$), (ii) $R_{\text{coarse}}^{\text{est}} \in [2.5, 4.0\ \mu\text{m}]$ ($\mathbf{Q} = \mathbf{Q}_1$), or (iii) $R_{\text{coarse}}^{\text{est}} >$ 4.0 μm ($\mathbf{Q} = \mathbf{Q}_2$). This feature leads to distortion both of V_{coarse} and $U_{\text{coarse}}(r)$. For fine particles, the relative

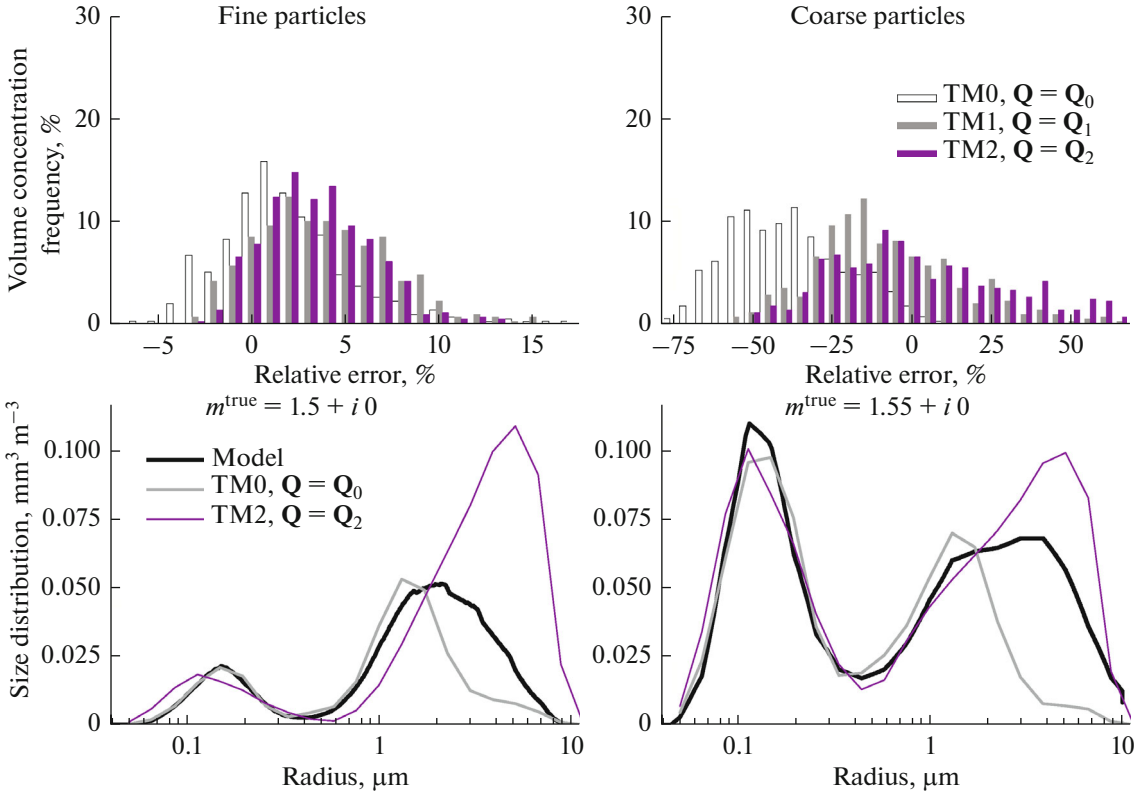

Fig. 1. Retrieval of the size distribution function by Tikhonov's regularization method for a known refractive index. Errors in estimating the particle concentration for the complete set of models (top), examples of SDF determination with different orders of stabilizer (4) for 2 empirical models of 462 (bottom).

error means (variances) ΔV_{fine} are 1.86% (3.39), $\mathbf{Q} = \mathbf{Q}_0$, or 3.33% (2.92), $\mathbf{Q} = \mathbf{Q}_2$; for coarse particles, they replaced by −38.15% (17.77), $\mathbf{Q} = \mathbf{Q}_0$, or 5.63% (37.62), $\mathbf{Q} = \mathbf{Q}_2$. Such pronounced bias of R_{coarse} and high values of ΔV_{coarse} are caused by information insufficiency of lidar measurements. Using (4) for a correct retrieval of $U_{\text{coarse}}(r)$ is not optimal even if the refractive index is known. The stabilizer requiring additional a priori information can be obtained from the preliminary estimate of R_{coarse}.

1.2. Statistical Regularization Method

Under the assumption of a normal distribution and independence of the vectors $\mathbf{u}$ and $\boldsymbol{\varepsilon}$, the solution of Eq. (3) obtained by the statistical regularization method can also be written in an explicit form [52]:

$$\mathbf{u} = (\mathbf{W}_u^{-1} + \mathbf{A}^{\mathrm{T}}\mathbf{W}_\varepsilon^{-1}\mathbf{A})^{-1}(\mathbf{A}^{\mathrm{T}}\mathbf{W}_\varepsilon^{-1}\mathbf{g} + \mathbf{W}_u^{-1}\mu_u). \qquad (5)$$

Mathematical expectations μ_u and μ_g of vectors $\mathbf{u}$ and $\mathbf{g}$ (under the assumption $\mu_\varepsilon = 0$) and the covariance (unnormalized correlation) matrices $\mathbf{W}_u$, $\mathbf{W}_\varepsilon$, and $\mathbf{W}_g$ must obey the equations

$$\mathbf{A}\mu_u = \mu_g, \quad \mathbf{A}\mathbf{W}_u\mathbf{A}^{\mathrm{T}} + \mathbf{W}_\varepsilon = \mathbf{W}_g. \qquad (6)$$

Let us assume that the signal error represents white noise; after the substitution $\mathbf{W}_\varepsilon = \sigma_\varepsilon^2\mathbf{I}$, solution Eq. (5) is transformed:

$$\mathbf{u} = (\mathbf{A}^{\mathrm{T}}\mathbf{A} + \alpha\mathbf{W}_u^{-1})^{-1}(\mathbf{A}^{\mathrm{T}}\mathbf{g} + \alpha\mathbf{W}_u^{-1}\mu_u), \qquad (7)$$

where $\alpha = \alpha(\sigma_\varepsilon)$ is the regularization parameter. Relationship (7) coincides with the optimal linear filtration; however, it is preferable, since the additional factor in the second term on the right side of the equation gives the asymptotic value for $u = \mu_u$ when $\alpha\mathbf{W}_u^{-1} \to \infty$.

The solution by Tikhonov's method also can be given by Eq. (7) if we use the stabilizer $\Omega[u - \mu_u]$. Obviously, in case of ill-posed initial Eq. (1), inversion of (6) for μ_u and $\mathbf{W}_u$ is also an ill-posed problem; however, requirements for the accuracy of estimating these parameters are much lower than for the accuracy of u retrieval. In this regard, simplified approximations of a priori moments can be used, and the less the number of free parameters, the more stable is the obtained solution.

Based on (7), one can construct algorithms invariant in the retrieval both of random and determined quantities. For the unique set of optical coefficients $\mathbf{g}$ (during the current session of observations), it is for-

mally (the unavailable components of the statistical ensemble are replaced by zeros) valid that

$$\boldsymbol{\mu}_g = \mathbf{g}, \quad \boldsymbol{\mu}_u = \mathbf{u}, \quad W_{u,ij} = u_i u_j \approx \delta_i \delta_j, \tag{8}$$

where $\boldsymbol{\delta} = \boldsymbol{\delta}_{\text{fine}} + \boldsymbol{\delta}_{\text{coarse}}$ is an estimate of the unknown $\mathbf{u}$. Relationship (8) allows one to determine $\mathbf{W}_u$ without any additional assumptions, to analyze stabilizer (7), and to distinguish its key parameters. The determinant $\det(\mathbf{W}_u) \equiv 0$; however, for calculating the inverse matrix in (7), it is admissible to use $\mathbf{W}_u(\gamma) = \mathbf{W}_u + \gamma\mathbf{I}$, $\gamma \approx 10^{-10}$. Analysis showed that first, an estimate of $\mathbf{W}_u$ can make it possible to consider the data on the presence of the two aerosol modes (in fact, on the presence of several extrema). Second, the elements located on the main and adjacent diagonals $\mathbf{W}_u^{-1}(\gamma)$ are sensitive to variations in the fine-particle parameters. For the parameters of coarse particle (R_{coarse} primarily), the sensitivity is manifested by the opposite elements, in the second and fourth quadrants of the image of $\mathbf{W}_u^{-1}(\gamma)$ [44, Fig. 4]. Neglecting these elements would again lead to the results shown in the bottom part of Fig. 1, even if the values on the main diagonal and two diagonals adjacent to it are set exactly. The obtained result is an idealization because the matrix $\mathbf{W}_u$ is calculated from the known $\mathbf{u}$. One of the possible ways of correct determination of the coarse-particle parameters is the replacement of the stabilizer by a simpler algorithm, without regularization and with quantitative estimation of the R_{coarse} value necessary under conditions of a priori uncertainty.

Let us represent the sought-for $\boldsymbol{\delta}$ as a sum of two sets, separately for fine $\boldsymbol{\delta}_{\text{fine}}$ and coarse $\boldsymbol{\delta}_{\text{coarse}}$ particles. The values $\boldsymbol{\delta}_{\text{fine}}$ can be found by Tikhonov's regularization method (4)—the stabilizer order does not influence the errors in $U_{\text{fine}}(r)$ (see Fig. 1). For the estimate of $\boldsymbol{\delta}_{\text{coarse}}$, we approximate $U_{\text{coarse}}(r)$ by the polynomial $b_0 + b_1 \ln r + b_2 (\ln r)^2$. Then, Eq. (3) is rewritten in the form

$$b_0\mathbf{l}_0 + b_1\mathbf{l}_1 + b_2\mathbf{l}_2 = \mathbf{g}_{\text{coarse}}, \tag{9}$$

where $\mathbf{l}_0 = \mathbf{A}_{\text{coarse}}\mathbf{e}$; $\mathbf{l}_1 = \mathbf{A}_{\text{coarse}}(\ln\mathbf{r})$; $\mathbf{l}_2 = \mathbf{A}_{\text{coarse}}(\ln\mathbf{r})^2$; $\mathbf{g}_{\text{coarse}} = \mathbf{g} - \mathbf{g}_{\text{fine}} = \mathbf{g} - \mathbf{A}_{\text{fine}}\boldsymbol{\delta}_{\text{fine}}$; $\mathbf{e}$ is a unit vector; and $\mathbf{r}$ is constructed from samples of expansion (2) for coarse particles. Solving (9) for the coefficients b_i is reduced to a solution of the system of three linear equations $\mathbf{Bb} = \mathbf{d}$, where components of the matrix $\mathbf{B}$ and the vector $\mathbf{d}$ can be represented in the form $B_{ik} = \sum_{j=1}^{5} \mathbf{l}_i\mathbf{l}_k$, $d_k = \sum_{j=1}^{5} \mathbf{g}_{\text{coarse}}\mathbf{l}_k$. If the coefficients b_i are known, the estimate of the average radius is determined from the formula

$$R_{\text{coarse}}^{\text{est}} \approx \exp(-0.5 b_1/b_2). \tag{10}$$

Estimate (10) is correct up to $R_* = 3$ μm (region I, $R_{\text{coarse}}^{\text{est}} \cong R_{\text{coarse}}^{\text{true}}$). However, it shifts toward higher values with increasing particle radius, increases uncontrollably (region II, $R_{\text{coarse}}^{\text{est}} > 3$ μm, $3 \le R_{\text{coarse}}^{\text{true}} \le 4.2$ μm), and fails to be observed at $R_{**} = 4.2$ μm. Then, its displacement toward smaller values is observed (region III, $R_{\text{coarse}}^{\text{est}} < 0.6$ μm, $R_{\text{coarse}}^{\text{true}} > 4.2$ μm) [44, Fig. 5]. The instability of estimating $R_{\text{coarse}}^{\text{true}} > 3$ μm is caused by features in the behavior of the efficiency factors (components of the matrix $\mathbf{A}_{\text{coarse}}$) and closeness of the coefficients b_1 and b_2. However, boundaries of the regions R_* and R_{**} are stable and almost independent of variations of the refractive index and other SDF parameters. Thus, $R_* = 3$ μm can be considered as the upper boundary of the correct estimate of R_{coarse} (and $U(r)$ itself) from lidar measurements. Below R_* (region I), μ_u and $\mathbf{W}_u$ in (7) can be preliminarily determined from the current set $\mathbf{g}$ according to (8). Since $\boldsymbol{\delta}_{\text{fine}}$ is retrieved uniquely, $\boldsymbol{\delta} \cong \mathbf{u}$, and the parabolic approximation of $U_{\text{coarse}}(r)$ yields correct estimates of R_{coarse} and $\boldsymbol{\delta}_{\text{coarse}}$. Above R_* (ranges II and III), relationship (10) allows one to determine only the variation range of the geometric mean radius. It is acceptable to use first moments of the ensemble of empirical models separated by values of R_{coarse}: 146 models of 462 at 3.36 μm (region II) or 104 models at 5.42 μm (region III). The sought-after function $U(r) = U_{\text{fine}}(r) + U_{\text{coarse}}(r)$ can be obtained from relationships (7) and (2).

Results of solving (3) by the statistical regularization method are presented in Fig. 2; the figure is similar to Fig. 1. The retrieval of $U(r)$ was carried out for the same set of models with different matrices $\mathbf{W}_u$: an a priori given (the SRM0 method, ensemble of the models with allowance for (10)), a known (SRM1, *current* observations), and an a posteriori estimated (SRM2, current observations/ensemble of models with allowance for (10)). Using SRM0 partially helps to reduce the bias of coarse-particle parameters. The difference between ranges of ΔV for different modes is preserved: for fine particles, the mean (variance) is 0.16% (2.39), and for coarse particles, 1.81% (27.20). In SRM1, matrix $\mathbf{W}_u$ is supposed to be known and is calculated by the known vector of the weight coefficients; for the matrix, the accuracies of estimating V_{fine} and V_{coarse} are comparable with the values of −0.16% (1.37) and −5.77% (2.20), respectively. A slight shift of profiles of $U_{\text{coarse}}(r)$ is caused by variations in $r_{\max}$ within the range of 7.5–10.0 μm. Thus, the "ideal" stabilizer does exist; in the next section it would allow us to investigate the details of estimating the complex refractive index. SRM2 is a result of using an approximate algorithm: $\mathbf{W}_u$ is a preliminarily retrieved for the coarse mode, which provides a correct retrieval of $U_{\text{coarse}}(r)$; the mean (variance) of ΔV_{coarse} is reduced to 2.75% (14.47). Two plausible sets μ_u and $\mathbf{W}_u$ represent all quantitative a priori information used. As a result,

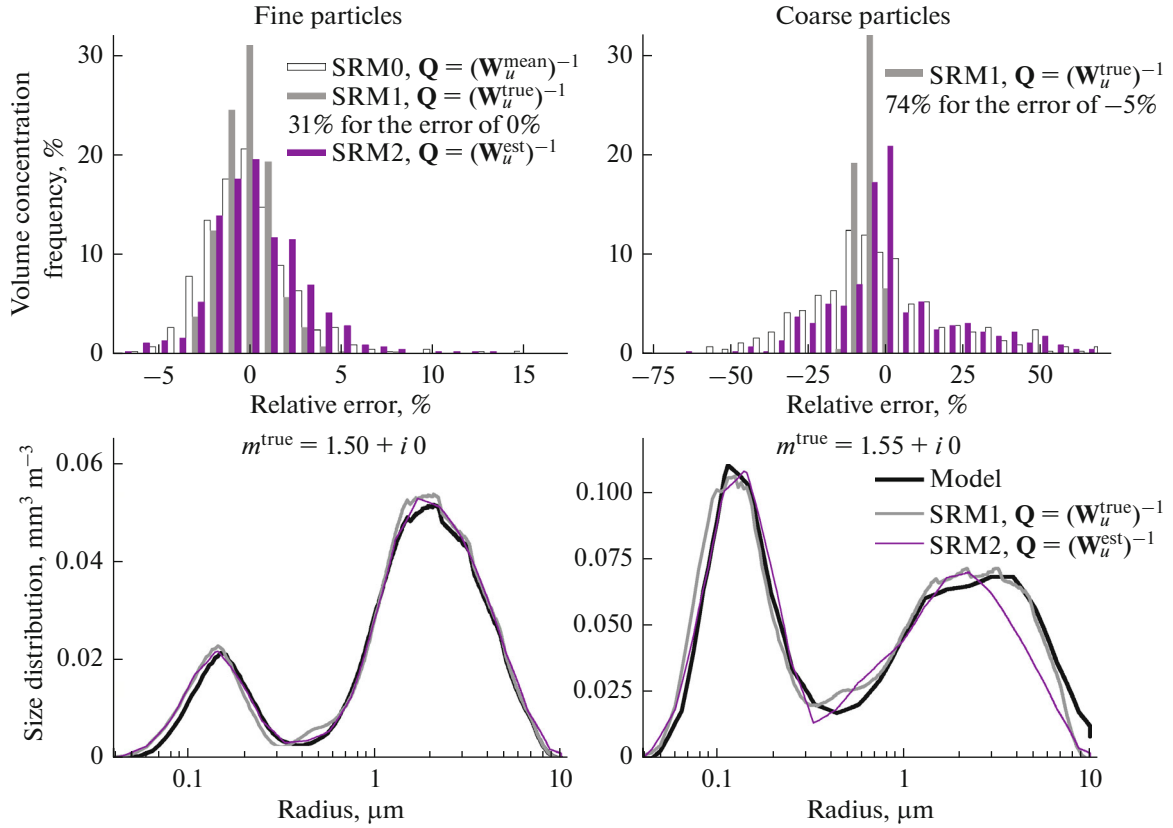

Fig. 2. Retrieval of the size distribution function by the statistical regularization method for a known refractive index. Errors in estimating the particle concentration for the complete set of models (top), examples of SDF determination with different covariance matrices of the sought-for solution for 2 empirical models of 462 (bottom).

an unbiased estimate of the concentration of coarse particles was obtained; due to the parabolic approximation to $R_{coarse}^{est} < 3$ μm it is even better than in the case of using SRM0. The SRM2 method is used as main in the next sections.

In the following sections we are going to demonstrate that errors in estimating the refractive index appear even in the case of an exactly determined distribution function. Also, we will show that the values of m are always localized inside the region M of low values of the functional: $\forall m\ \Phi(m) \le E(\varepsilon^{meas} + \varepsilon^{math}) < \varepsilon^{meas}$, and their location is due to absorption.

2. RECONSTRUCTION OF THE REFRACTIVE INDEX

The problem of determination the complex refractive index is reduced to direct minimization of the discrepancy functional [29, 33, 37, 38, 45, 46]

$$\Phi_1(m) = \left\| g_j^{meas} - g_j^{calc}(m) \right\| = \frac{1}{5}\sum_{j=1}^{5} \frac{\left| g_j^{meas} - g_j^{calc}(m) \right|}{g_j^{meas}} \times 100\%. \quad (11)$$

On the one hand, it depends on the measured optical coefficients g_j^{meas}; on the other hand, on the values of these coefficients calculated from the reconstructed microphysical characteristics, $g_j^{calc}(m)$. The relative error in (11) is quite useful, since the coefficients σ and β have different dimensionalities.

In the case of lidar measurements, the information content of optical coefficients is predefined by the characteristics of their Mie efficiencies (e.g., see Fig. 1 [29]). The extinction coefficients, depending on scattering and absorption, ensure a correct estimation of SDF for particles < 1 μm. The backscattering coefficients determine its reconstruction above 1 μm. Moreover, in the cases of fixed m_{real} and $U(r)$ an increase in m_{image} gives rise to an appreciable decrease in β, while it hardly affects σ. The spectral variation of the lidar ratio σ/β is sensitive to CRI. A concurrent use of optical characteristics offers a possibility of estimating m and $U(r)$ simultaneously.

Direct minimization of the functional (the lookup table method) is based on searching for minimum values of $\Phi(m)$ on the plane (m_{real}, m_{image}) of all physically justified values of refractive index components and without any additional a priori assumptions. If errors

are absent, there is a single minimum $\Phi(m) \equiv 0$ for any refractive index. The presence of noise distorts the surface of the functional and leads to the appearance of additional, so-called false, minima. Their position on the plane is not random: the minima of $\Phi(m)$ are localized inside the region M and any of the local minima can turn out to be global. It is the case a probable invalidity of the global minimum giving rise to a possible bias in the refractive index parts.

In the second series of numerical experiments, errors in estimating the refractive index are studied for the known (SRM1) or determined (SRM2) distribution function. When m and $U(r)$ are reconstructed simultaneously, the required expenditures of computer time are larger approximately by $N_{\text{real}}N_{\text{image}}$ times, where $N_{\text{real}} = N(m_{\text{real}})$ and $N_{\text{image}} = N(m_{\text{image}})$ are numbers of points in the ordinate and abscissa of the CRI. Therefore, for each of eight values $m_{\text{image}}^{\text{true}} = 0$, 0.001, 0.006, 0.01, 0.02, 0.04, 0.06, and 0.1 g_j^{meas} is calculated for first 50 empirical models $U^{\text{true}}(r)$ of 462 with the same varying values $m_{\text{real}}^{\text{true}} = 1.50$ (13 models), 1.55 (13), 1.60 (12), and 1.65 (12). Resolution possibilities of the determination of microphysical characteristics are considered on 400 models, $400 = 8(m_{\text{image}}^{\text{true}}) \times 50\left(U^{\text{true}}(r) + m_{\text{real}}^{\text{true}}\right)$.

2.1. Estimation of the Refractive Index in the Absence of Absorption

The algorithm for determining the refractive index components and simultaneous reconstruction of the distribution function contains several stages. In every point on (m_{real}, m_{image}), kernels of Eq. (1) are calculated, $U^{\text{est}}(r)$ is estimated accordance with (7) or (4), and the value of the discrepancy functional is determined from (11). On the entire plane there is only one correct set of $m^{\text{est}} + U^{\text{est}}(r)$ out of $N = N_{\text{real}}N_{\text{image}}$; it invariably falls within the region M of low values of $\Phi_1(m)$. The problem is thought to be solved correctly if this set corresponds to the global minimum of the functional. At the same time, one value of the first component, either m_{real} or m_{image}, has a single corresponding minimum in the entire range of the second component, either m_{image} or m_{real}. Any of the local minima (it is not improbable that it could be false) could also be localized inside the region M. If one of the CRI components can be determined correctly, the error in estimating the second one is small, and the use of the global minimum of $\Phi_1(m)$ is quite appropriate. Fortunately, the real part is retrieved correctly at weak absorption. Moreover, it is suitable to analyze a deviation of the model value from the reconstructed value, $\delta m = m^{\text{est}} - m^{\text{true}}$. The criterion of relative errors is not very effective since the variation range of m_{real} is several percent and the imaginary part can be set equal to zero.

The reconstruction of the refractive index components for $m_{\text{image}}^{\text{true}} = 0$ is presented in Fig. 3. The CRI was calculated from two grids using the logarithmic scale for m_{image}:

Grid 1a, detailed real part, Figs. 3 (top) and 4 (left): a set of $m_{\text{real}} \in [1.35, 1.65]$ with the partition 0.01, $N_{\text{real}} = 30$ points for fixed m_{image} and $m_{\text{image}} = 0.0001$, 0.0005, 0.001, 0.005, 0.01, 0.05, 0.1, $N_{\text{image}} = 7$ points for fixed m_{real}, $N = N_{\text{real}}N_{\text{image}} = 210$ points altogether.

Grid 1b, detailed imaginary part, Fig. 3 (bottom) and 4 (right): a set of $m_{\text{real}} \in [1.35, 1.65]$ with the partition 0.05, $N_{\text{real}} = 7$ points for fixed m_{image} and $m_{\text{image}} = 0.0001, 0.0002, ..., 0.001, 0.002, ..., 0.01, 0.02, ..., 0.1$, $N_{\text{image}} = 30$ points for fixed m_{real}, $N = N_{\text{real}}N_{\text{image}} = 210$ points altogether.

Every column of the bar chart indicates for how many implementations (in percentage relative to 50 models for one $m_{\text{image}}^{\text{true}}$) the error in estimating the components of m falls within this range.

At $m_{\text{image}}^{\text{true}} \equiv 0$, local minima of the functional are located along the axis of m_{image}. The right panel of Fig. 3 illustrates the variation range of the imaginary part itself, $\delta m_{\text{image}} = m_{\text{image}}^{\text{est}} - m_{\text{image}}^{\text{true}} \equiv m_{\text{image}}^{\text{est}}$. The left panel of Fig. 3 shows errors of estimating the real part, $\delta m_{\text{real}} = m_{\text{real}}^{\text{est}} - m_{\text{real}}^{\text{true}}$. At the global minimum $m_{\text{real}}^{\text{est}} \cong m_{\text{real}}^{\text{true}}$, the real part is reconstructed correctly. The mean deviation δm over 50 models (and mean relative error Δm) amounts to -0.0002 (-0.024%) for the real component and $+0.0015$ ($\infty\%$, i.e., cannot be determined) for the imaginary component. The deviation δm_{real} is quite acceptable during determination of the 'true' type in the course of identification of the scattering aerosol at different altitudes [26, 28, 29].

The joint determination of the microphysical characteristics has been performed using two algorithms for the SDF retrieval. A comparison of the results, obtained with the exact SRM1 ($\varepsilon^{\text{math}} = 0$, $\varepsilon^{\text{meas}} \neq 0$) and approximate SRM2 ($\varepsilon^{\text{math}} \neq 0$, $\varepsilon^{\text{meas}} \neq 0$), illustrates the influence of mathematical errors on the values of the discrepancy functional. Since the errors in estimating the CRI components are close to each other in both methods, one can argue that the global minimum primarily shifts due to an ambiguity of reconstruction of m. In what follows, only the SRM2 algorithm is used. In the next section, we will investigate the influence of the aerosol absorption properties on the correct estimation of the refractive index. Possible errors of determining $U(r)$ will be presented at the end of Section 3.

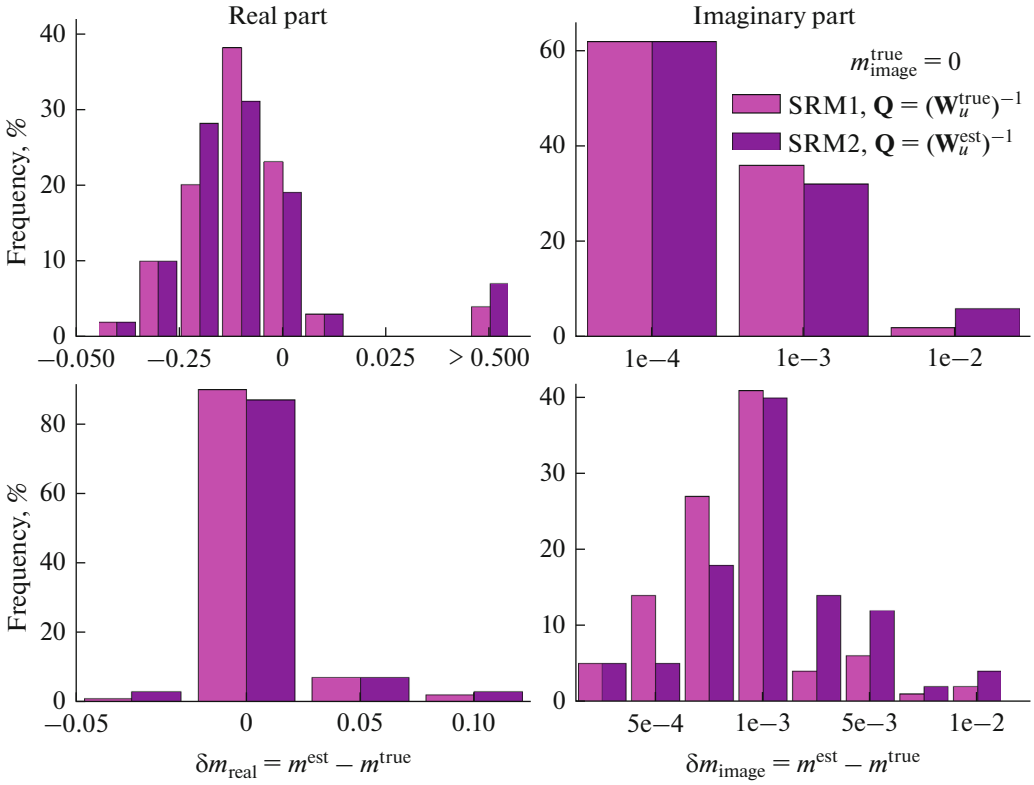

Fig. 3. Errors of refractive index reconstruction in the absence of absorption (during a simultaneous determination of CRI + SDF). Functional (11) is minimized using grids *Ia* (top) or *Ib* (bottom). At each point of the grid, $U(r)$ is retrieved by the statistical regularization method with different covariance matrices of the sought-for solution.

2.2. Estimation of the Refractive Index in the Presence of Absorption

According to [45], if $\varepsilon^{\text{math}} = 0$ and $\varepsilon^{\text{meas}} \neq 0$ are satisfied (in fact, the SRM1 method for the SDF), lidar measurements allow one to correctly estimate m within the absorption interval from 0.0001 to 0.1. Close values of the functional at local minima can also manifest themselves for average absorption; in particular, it was shown in [38, p. 2191]. If $\varepsilon^{\text{math}} \neq 0$ and $\varepsilon^{\text{meas}} = 0$ are used, the local minima $m^{\text{est}} = m^{\text{true}} = 1.5 + i \times 0.015$ (B), $m^{\text{est}} = 1.472 + i \times 0.008$ (B.1), and $m^{\text{est}} = 1.639 + i \times 0.041$ (B.2) correspond to common values of the optical coefficients and region M with functional values <0.1. However, both abovementioned versions of noise are an idealization. Below, the behavior of local minima is considered under conditions of real measurements, at $\varepsilon^{\text{meas}} \neq 0$ and $\varepsilon^{\text{math}} \neq 0$. When $m_{\text{image}}^{\text{true}} > 0.1$, the behavior of the kernels (1) gives rise to an incorrect retrieval of the distribution function: the information on coarse particles is lost and so is even the separation into fractions. It is for this reason that we do not deal with the values of $m_{\text{image}} > 0.1$ in the present work. Features of the change in kernels of system (1) with an increase in absorption for spherical particles were presented in more detail in [28, Sections 2 and 3].

The refractive index reconstruction for the eight values of $m_{\text{image}}^{\text{true}}$, i.e., for all 400 numerical models, is given in the top part of Fig. 4. The left panel of Fig. 4 illustrates the errors in estimating the real part; the right panel, for the imaginary part. A deviation of the model value from the reconstructed value is assumed to be correct at $|\delta m_{\text{real}}| < 0.025$ and $|\delta m_{\text{image}}| < 0.0025$. The values $|\delta m_{\text{real}}| \geq 0.025$ and $|\delta m_{\text{image}}| \geq 0.0025$ illustrate the ranges of incorrect m^{est}.

Analysis allows one to distinguish some features in reconstructing the refractive index. The variation range of absorption (due to the variation of CRI determination errors) can be conventionally divided into three regions: $m_{\text{image}}^{\text{true}} < 0.01$ (weak absorption), $m_{\text{image}}^{\text{true}} \in [0.01, 0.04]$ (middle absorption), and $0.04 < m_{\text{image}}^{\text{true}} \leq 0.1$ (strong absorption). For the first region, the validity of using the global maximum (11) is justified, $m_{\text{real}}^{\text{est}} \cong m_{\text{real}}^{\text{true}}$, similar to the case of weakly absorbing particles discussed in Subsection 2.1. With increasing absorption, the domain of the minima is smoothed. This gives rise to an uncertainty in estimating the refractive index, which is quite conspicuous in a limited range $m_{\text{image}}^{\text{true}} \in [0.01, 0.04]$. Peculiarities of the kernel change in the second region do not manifest themselves. The further

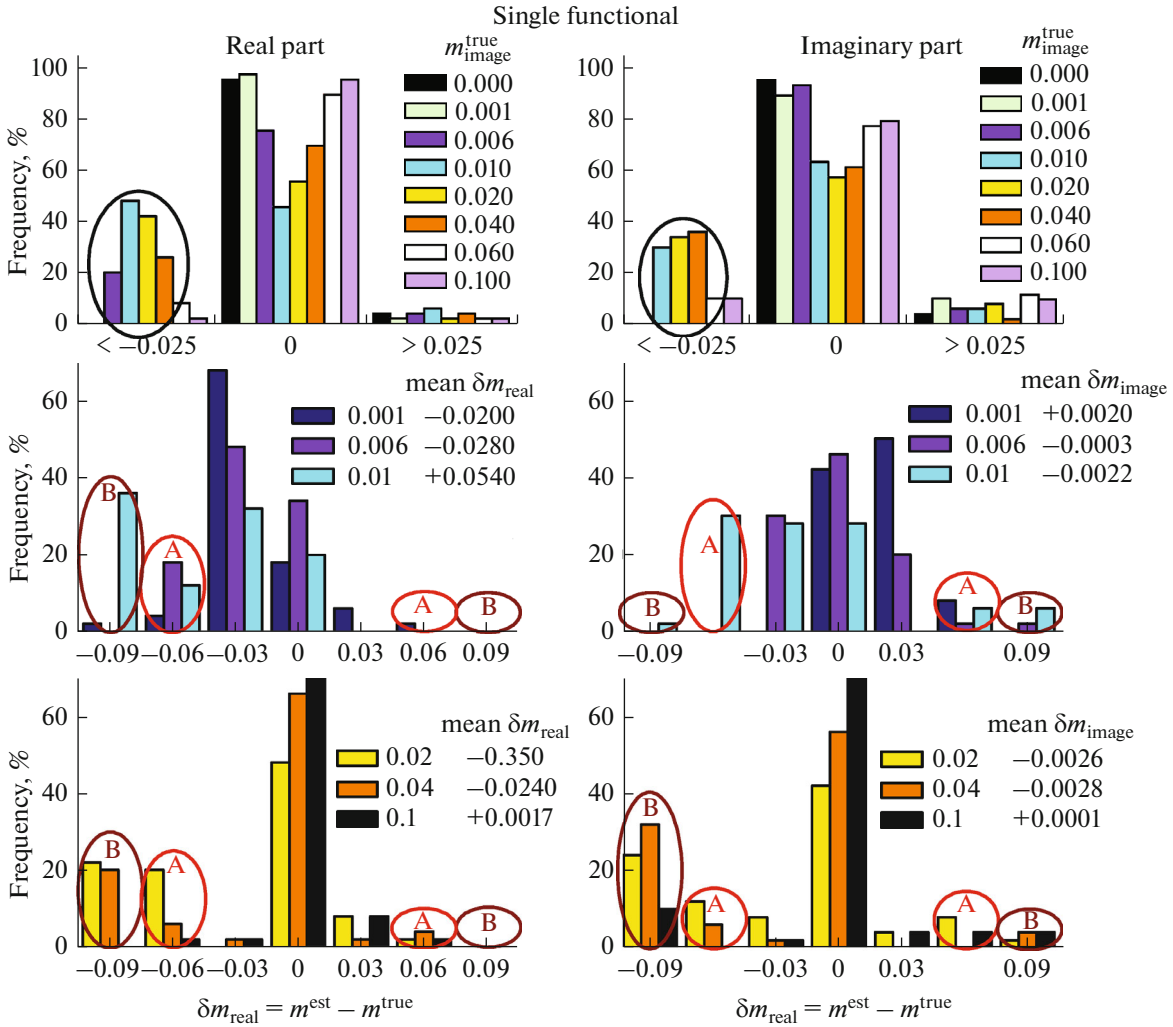

Fig. 4. Variations in errors of the refractive index reconstruction with increasing absorption, CRI + SDF simultaneously, at a single functional: differences between the model and retrieved m, each value of absorption m_{image}^{true} involves 50 models $\left(U^{true}(r) + m_{real}^{true}\right)$ (top); detailed changes in δm at weak (center) or strong absorption (bottom).

increasing absorption leads to a decrease in the difference between m^{true} and m^{est} and, in the third region, using the global minimum of $\Phi_1(m)$ is allowed, $m_{image}^{est} \cong m_{image}^{true}$.

The cause of CRI uncertainty in the second region can be understood by interpreting results illustrated by the middle and bottom panels of Fig. 4; $m_{image}^{true} = 0.001$, 0.006, 0.01 and $m_{image}^{true} = 0.02$, 0.04, 0.1, respectively. The edge columns with values of ±0.06, ±0.09 (m_{real}) or ±0.006, ±0.009 (m_{image}) in the abscissa demonstrate "bad" estimates with errors $0.045 \le |\delta m_{real}| < 0.075$, $0.0045 \le |\delta m_{image}| < 0.0075$ (zones A) or "very bad" ones, $|\delta m_{real}| > 0.075$, $|\delta m_{image}| > 0.0075$ (zones B). For small absorption $m_{image}^{true} = 0$ (see Fig. 3) or 0.001 (central panel of Fig. 4), local minima $\Phi_1(m)$ are next to the sought-for m^{true}. Errors in estimating the CRI are comparable in the position of components (negative δm_{real} and positive δm_{image}) and in their magnitudes. With increasing absorption, the region M changes: for $m_{image}^{true} = 0.006$, the deviation δm increases due to the manifestation of a false global minimum for some models with $m_{real}^{true} = 1.50$; zones A in the middle part of Fig. 4 correspond to them. When $m_{image}^{true} = 0.02$, the false minima for models with $m_{real}^{true} = 1.50$ disappear; they are preserved for other three values and lead to maximal errors of m_{image}^{est} (bottom panel of Fig. 4). If $m_{image}^{true} = 0.04$, the false minimum can become global

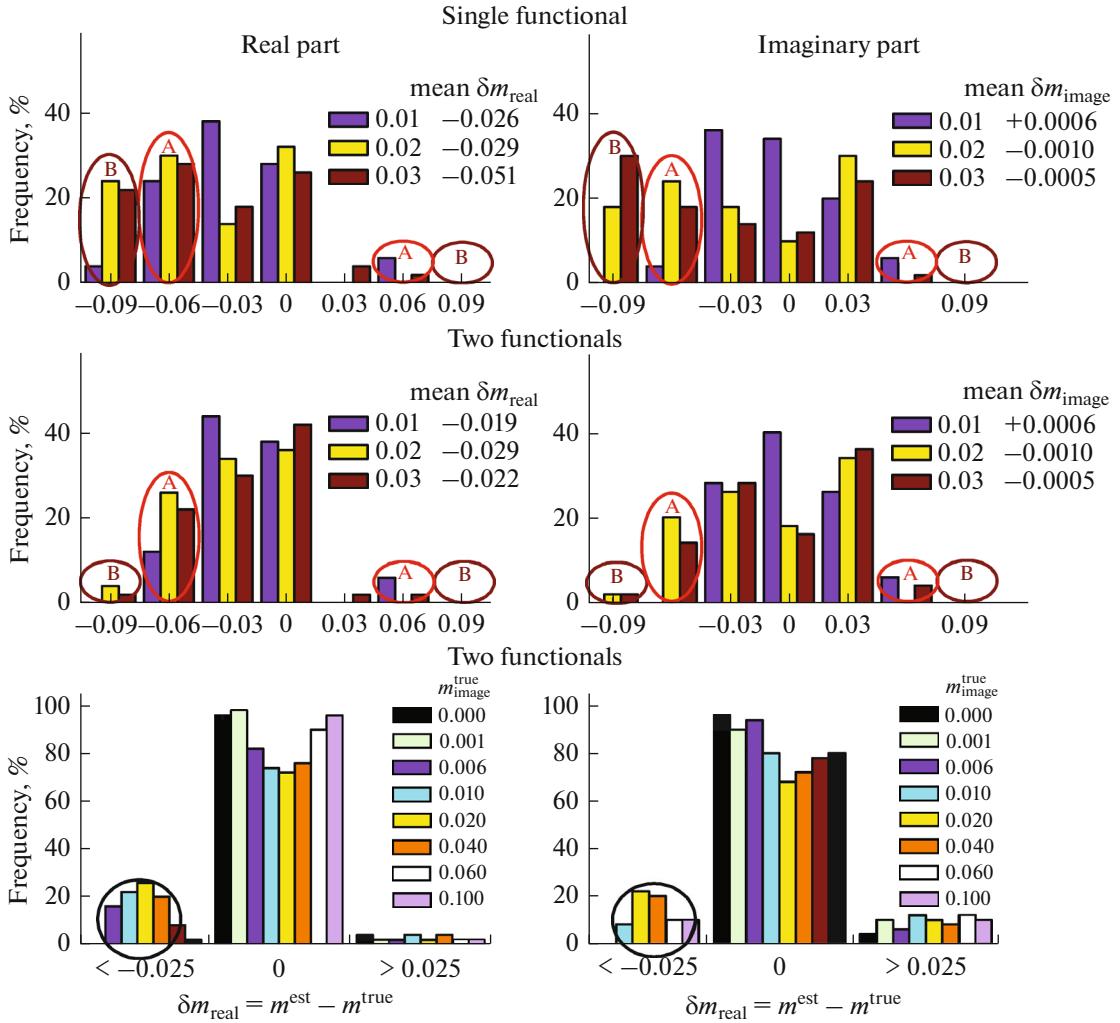

Fig. 5. Influence of used functionals on the reconstruction of the refractive index, CRI + SDF simultaneously. Detailed variations in δm for a one (top) or two (center) functionals, mean absorption; differences between the model and retrieved m at combined $\Phi_1(m)$ and $\Phi_2(m)$, each value of absorption $m_{\text{real}}^{\text{true}}$ involves 50 models $\left(U^{\text{true}}(r) + m_{\text{real}}^{\text{true}}\right)$ (bottom).

only for $m_{\text{real}}^{\text{true}} = 1.65$, the results are presented mainly in zones B. Absorptions at $m_{\text{image}}^{\text{true}} = 0.006$ or 0.04 are, in some specified sense, synonymous; the means $\delta m_{\text{real}} = -0.028$ or -0.024 coincide. A considerable (almost by an order of magnitude) difference manifests itself for the imaginary component, $\delta m_{\text{image}} = -0.0003$ or -0.0028. Since the absorption values themselves differ almost by an order of magnitude, maybe the errors are due to inadequate decomposition of the CRI in the logarithmic scale of m_{image}.

Reconstruction of the refractive index components is also presented in Fig. 5. The CRI is calculated using the linear scale for m_{image}; other parameters of grids *1a*, *1b* and *2a*, *2b* are comparable:

Grid 2a, detailed real part, Fig. 5 (left): a set of $m_{\text{real}} \in [1.35, 1.65]$ with the partition of 0.02, $N_{\text{real}} = 16$ points for fixed m_{image}; $m_{\text{image}} \in [0, 0.05]$ with the partition of 0.005, $N_{\text{image}} = 11$ points for fixed m_{real}; totally, $N = N_{\text{real}}N_{\text{image}} = 176$ points altogether;

Grid 2b, detailed imaginary part, Fig. 5 (right): a set of $m_{\text{real}} \in [1.35, 1.65]$ with the partition of 0.05, $N_{\text{real}} = 7$ points for fixed m_{image}; $m_{\text{image}} \in [0, 0.05]$ with the partition of 0.002, $N_{\text{image}} = 26$ points for fixed m_{real}; totally, $N = N_{\text{real}}N_{\text{image}} = 182$ points altogether.

The central and edge columns in the top panel of Fig. 5 demonstrate good and bad estimates with errors $|\delta m_{\text{real}}| < 0.045$, $|\delta m_{\text{image}}| < 0.0045$ or $|\delta m_{\text{real}}| \geq 0.045$, $|\delta m_{\text{image}}| \geq 0.0045$. In the absorption region $m_{\text{image}}^{\text{true}} \leq 0.015$, it makes sense to use a linear scale of m_{image}, since the values within $0.01 < m_{\text{image}}^{\text{est}} < 0.02$ are not taken into consideration. In particular, at $m_{\text{image}}^{\text{true}} =$

0.01, average values δm over 50 models decrease by an order of magnitude for the imaginary part and by a factor of two for the real part. However, if $m_{\text{image}}^{\text{true}} = 0.02$ or 0.03, the choice of the scale or the grid does not exert any influence, and the shift of both parts of m^{est} persists. Within the range $0.15 < m_{\text{image}}^{\text{true}} < 0.04$ (so-called mean absorption), the local minima $\Phi_1(m)$ are weakly discernible, which leads to maximal errors in reconstructing the CRI from nighttime lidar measurements.

It is possible to modify the boundaries of the sought-for refractive index or to select a step for its imaginary part in grids of the *1a*, *1b* or *2a*, *2b* type. However, another approach is more effective—constriction the range of allowable values of m by increasing the number of used functionals.

3. SIMULTANEOUS DETERMINATION OF BOTH MICROPHYSICAL CHARACTERISTICS

It is expedient to compare different discrepancy functionals, e.g., those depending on all optical coefficients (11) (or on the spectral behavior of σ/β [45]) or only on Ångström exponent (A) for the backscattering coefficients:

$$\Phi_2(m) = 0.5\sum_{j=1}^{2}\frac{\left|A_j^{\text{meas}} - A_j^{\text{calc}}(m)\right|}{A_j^{\text{meas}}}\times 100\%. \qquad (12)$$

In the global minimum, the functionals yield close values of one of the CRI components: $m_{\text{real}}^{\text{est}}(\Phi_1) \approx m_{\text{real}}^{\text{est}}(\Phi_2)$ (weak absorption) and $m_{\text{image}}^{\text{est}}(\Phi_1) \approx m_{\text{image}}^{\text{est}}(\Phi_2)$ (strong absorption). The absence of coinciding values of $\Phi_i(m)$ is particularly evident for the mean absorption. The region of minima (11) appears during a simultaneous increase of the CRI parts, and in accordance with (12)—in the course of decreasing m_{real} with increasing m_{image}. Regions of localization of low values of both functionals for real lidar measurements are presented in more detail in [53, Fig. 2].

Reconstruction of CRI + SDF according to (11) was described in Subsection 2.1; the algorithm for minimizing $\Phi_2(m)$ is similar, relationship (11) has changed to (12). To compare the functional defined by the same grid, it is sufficient to consider only the local minima; its position on the plane of the CRI values principally differs. Neglecting absolute values of $\Phi_i(m)$—in fact, the equal status of all minima—makes it possible to distinguish the zone of their intersection on the (m_{real}, m_{image}) plane and to narrow the domain of the refractive index.

Features of the CRI determination are presented in the top and middle panels of Fig. 5. The difference between the $\Phi_1(m)$ and $\Phi_1(m) + \Phi_2(m)$ methods leads to a noncoincidence of regions where m^{est} is estimated incorrectly. For $m_{\text{image}}^{\text{true}} = 0.02$ and 0.03, one functional yields an approximately equal volume of bad ($0.045 \le |\delta m_{\text{real}}| < 0.075$, $0.0045 \le |\delta m_{\text{image}}| < 0.0075$) and very bad ($|\delta m_{\text{real}}| > 0.075$, $|\delta m_{\text{image}}| > 0.0075$) errors. For two functionals, the contribution of zones A decreases and the contribution of zones B is almost completely annihilated. As a result, values of δm_{image} averaged over 50 models decrease by a factor of three (from -0.0032 to -0.0010) for $m_{\text{image}}^{\text{true}} = 0.02$ and by a factor of seven (from -0.0036 to -0.0006) for $m_{\text{image}}^{\text{true}} = 0.03$.

The options of using the functionals (11) + (12) are presented in the bottom part of Fig. 5; the result is comparable with the top panel of Fig. 4. Note that at $m_{\text{image}}^{\text{true}} \in [0.01, 0.04]$ 'hitting' the false minimum decreases from 40% to 20%. Moreover, a combined, simultaneous use of two $\Phi(m)$ would result in a more correct estimation of m. A deviation of the model value from the reconstructed value corresponds to $0.025 \le |\delta m_{\text{real}}| < 0.150$ and $0.0025 \le |\delta m_{\text{image}}| < 0.0150$ for $\Phi_1(m)$ or $0.025 \le |\delta m_{\text{real}}| < 0.075$ and $0.0025 \le |\delta m_{\text{image}}| < 0.0075$ for $\Phi_1(m) + \Phi_2(m)$.

Let us demonstrate the potential of estimating the size distribution functions by the SRM2 algorithm under conditions of an expected uncertainty. The top panel of Fig. 6 illustrates the errors of the volume concentrations of the SDF modes. Its structure is similar to [44, Fig. 6], but for the case of a concurrent estimation of the refractive index for $8(m_{\text{image}}^{\text{true}}) \times 50\left(U^{\text{true}}(r) + m_{\text{real}}^{\text{true}}\right) = 400$ models. In view of the fact that the accuracy of determination of the fine fraction is essentially higher, the step of the histograms is 2% (V_{fine}) and 5% (V_{coarse}). The deformation of the fine mode is consistent with the variation range of incorrect m^{est}. If m is known and only (7) + (2) is used, the mean (variance) of ΔV_{fine} amount to -1.06% (2.86) for $m_{\text{image}}^{\text{true}} = 0.02$ and 50 models $U^{\text{true}}(r) + m_{\text{real}}^{\text{true}}$. When m is estimated, ΔV_{fine} increase to 11.26% (10.60), (11) + (7) + (2), or to 9.18% (3.43), (11) + (12) + (7) + (2). The joint use of $\Phi_1(m)$ and $\Phi_2(m)$ decreases the difference between the model and reconstructed m and leads to a lesser deformation of $U(r)$. For the coarse mode, ΔV_{coarse} change weakly and amount either to -4.09% (22.1), (7) + (2), or to -6.68% (26.7), (11) + (7) + (2), or to -6.80% (24.3), (11) + (12) + (7) + (2). Correctness of $U_{\text{coarse}}(r)$ estimation for the lidar is determined to a greater extent by the choice of the stabilizer using (7) + (2) or (4) + (2).

The bottom panel of Fig. 6 demonstrates how the shape of $U(r)$ changes in the two models (for the given m they are presented in Figs. 1 and 2) in the local minima of the functional. The bottom left part of Fig. 6 illustrates a "simple" case, the global minimum of (11) coincides with one of local minima of (11) and (12). The bottom right part of Fig. 6 shows a "complicated" case, m^{true} and m^{est} are noticeably different for (11).

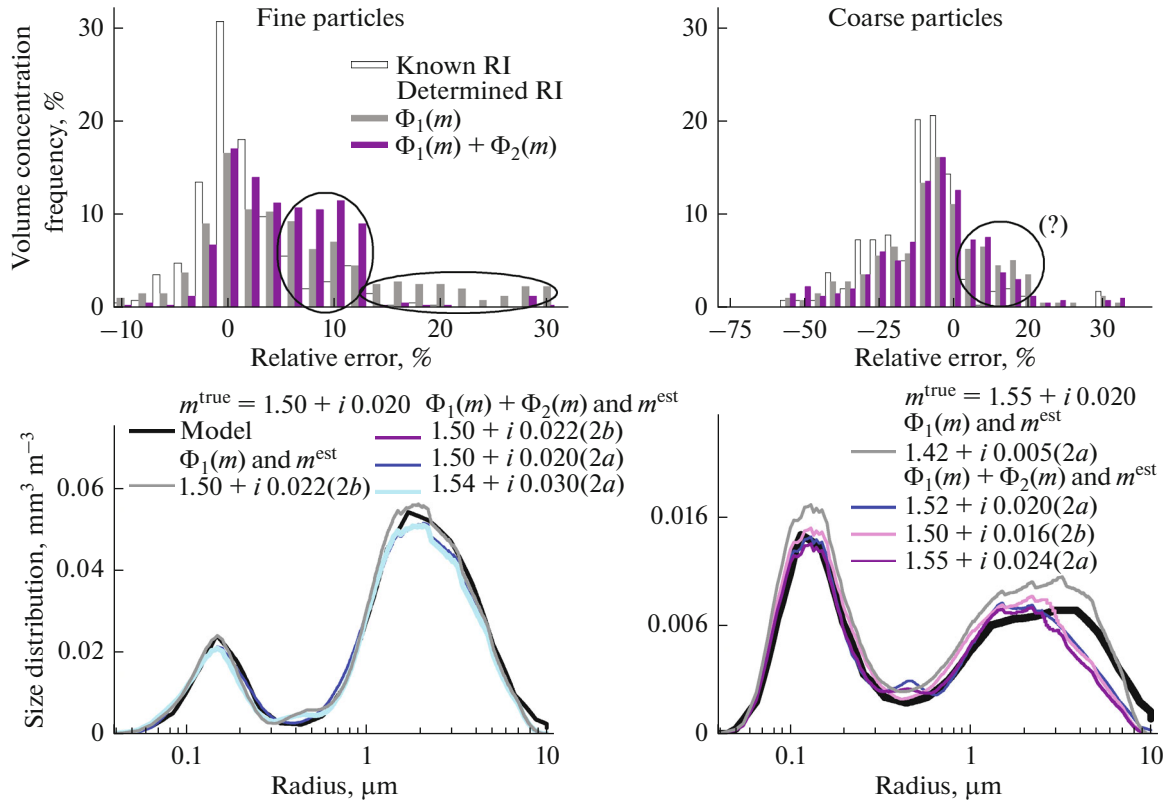

Fig. 6. Influence of used functionals on the retrieval of the size distribution function, CRI + SDF simultaneously. On the top, errors in estimating the particle concentration, each value of absorption m_{real}^{true} involves 50 models $\left(U^{true}(r) + m_{real}^{true}\right)$; on the bottom, examples of SDF determination in local minima of different functionals for 2 empirical models of 50.

The superposition of (11) and (12) yields a better retrieval of $U(r)$: the decrease of the CRI domain restricts the range of allowable values of (3). Correct kernels of (1) provide a physically justified variation range of **u** and leads to the sought-for distribution function. The statistical regularization method gives an admissible estimate of $U(r)$ for the mean radius $R_{coarse}^{est} \notin [0.6, 3.0\ \mu m]$ (see Subsection 1.2). Thus, the simultaneous reconstruction of CRI + SDF provides the plausible retrieval of the size distribution function from nighttime lidar measurements. For the complex refractive index, the inverse problem is more complicated and is still not solved completely.

Theoretical aspects of interpreting AERONET measurements were presented in [24, 54]. The main input parameters of the inverse problem are the data on the measured coefficients of directed light scattering in the angular range from 2° to 140° (including the aureole part up to 10°). The errors of the refractive index estimation differ. The real part can be retrieved with a high accuracy, and we can discard its spectral behavior. The imaginary part is estimated correctly if it has: (i) weak spectral selectivity and (ii) does not vary in the regions of low absolute values, $m_{image}^{true} < 0.005$. Large errors in estimating m_{image} are due to the absence of the information in the rear hemisphere of the scattering phase function, 140°–180°. The lower boundary for the correct estimation of the imaginary part with the use of lidar measurements is less by an order of magnitude, as shown in Subsection 2.1. Recall that we recommend experts on inverse problems comparing different discrepancy functionals.

CONCLUSIONS

The methodical specifics of combined, simultaneous determination of microphysical characteristics from the lidar measurements of extinction (355 and 532 nm) and backscattering (355, 532, and 1064 nm) coefficients have been discussed. The results demonstrate that there are two serious obstacles to reconstructing the microphysical characteristics: (i) biased estimation of SDF parameters for the coarse particles and (ii) ambiguity of determination of CRI proper. Both problems are caused by the information content of lidar measurements. Solution of the first problem provides an adequate selection of the regularization method for the SDF retrieval. The second problem unfortunately does not allow determining the spectral dynamics of the CRI but permits obtaining a reconstruction of its average value.

The lidar provides the determination of both components of the refractive index related to kernels of the Fredholm's equations in a limited range at $m_{real} \in [1.35, 1.65]$ and $m_{image} \in [0.0001, 0.1]$. The variation range of absorption (or the imaginary part of m) can be conventionally divided into three sections: $m_{image} < 0.01$, $m_{image} \in [0.01, 0.04]$, and $0.04 < m_{image} \le 0.1$. This separation is due to the smoothing of the discrepancy functional and broadening of its local minima on the (m_{real}, m_{image}) plane, which gives rise to ambiguity of determining the CRI—a false minimum could appear to be global. For the first section, using the global minimum is justified because the minima are situated near the sought-for m. In the third section, on the contrary, they go beyond the boundaries of physically justified values of the refractive index and the problem is solved uniquely. There is a challenge in the midsection: a probable invalidity of the global minimum gives rise to a possible bias in the refractive index parts. It should be underlined that a choice of a single $\Phi(m)$ only is not sufficient for the second section. One more functional based on another set of optical coefficients and providing principally different positions of the local minima on the (m_{real}, m_{image}) plane is necessary. Superposition of two $\Phi_i(m)$ leads to a restriction of the CRI domain and, correspondingly, to a more correct estimate of m. Differently directed possibilities in the determination of the complex refractive index call for further considerations.

FUNDING

This work was supported in part by the Russian Foundation for Basic Research and Tomsk oblast (project no. 19-48-700014) in regard to theoretical investigations. The empirical material was obtained under financial support of project no. AAAA-A17-117021310142-5.

The author would like to give tribute to the memory of M.A. Sviridenkov. Section 1 and Subsection 2.1 are the result of our joint work.

CONFLICT OF INTEREST

The author declares that she has no conflicts of interest.

REFERENCES

1. L. A. Remer, Y. J. Kaufman, D. Tanre, S. Mattoo, D. A. Chu, J. V. Martins, R.-R. Li, C. Ichoku, R. C. Levi, R. G. Kleidman, T. F. Eck, E. Vermote, and B. N. Holben, "The MODIS aerosol algorithm, products, and validation," J. Atmos. Sci. **62**, 947–973 (2005).
2. D. Tanre, F. M. Breon, J. L. Deuse, O. Dubovik, F. Ducos, P. Francois, P. Goloub, M. Herman, A. Lifermann, and F. Waquet, "Remote sensing of aerosol by using polarized, directional and spectral measurements within the A-Train: The PARASOL mission," Atmos. Meas. Tech. Discuss. **4**, 2037–2069 (2011).
3. D. M. Winker, M. A. Vaughan, A. Omar, Y. Hu, K. A. Powell, Z. Liu, W. H. Hunt, and S. A. Young, "Overview of the CALIPSO Mission and CALIOP data processing algorithms," J. Atmos. Ocean. Technol. **26**, 2310–2323 (2009).
4. B. N. Holben, T. F. Eck, I. Slutsker, D. Tanre, J. P. Buis, A. Setzer, E. Vermote, J. A. Reagan, Y. Kaufman, T. Nakajima, F. Lavenu, I. Jankowiak, and A. Smirnov, "AERONET—a federated instrument network and data archive for aerosol characterization," Remote Sens. Environ. **66**, 1–16 (1998).
5. O. V. Dubovik, T. V. Lapyonok, and S. L. Oshchepkov, "Improved technique for data inversion: Optical sizing of multicomponent aerosols," Appl. Opt. **34**, 8422–8436 (1995).
6. O. V. Dubovik and M. D. King, "A flexible inversion algorithm for retrieval of aerosol optical properties from sun and sky radiance measurements," J. Geophys. Res. **105**, 20 673–20 696 (2000).
7. J. Bosenberg, A. Ansmann, J. M. Baldasano, D. Balis, C. Bockmann, B. Calpini, A. Chaikovsky, P. Flamant, A. Hagard, V. Mitev, A. Papayannis, J. Pelon, D. Resendes, J. Schneider, N. Spinelli, T. Trickl, G. Vaughan, G. Visconti, and M. Wiegner, "EARLINET: A European aerosol research lidar network," in *Advances in Laser Remote Sensing*, Ed. by A. Dabas, C. Loth, and J. Pelon (Editions de L'Ecole Polytechnique, 2000), p. 155–158.
8. T. Murayama, N. Sugimoto, I. Uno, K. Kinoshita, K. Aoki, N. Hagiwara, Z. Liu, I. Matsui, T. Sakai, T. Shibata, K. Arao, B.-J. Sohn, J.-G. Won, S.-C. Yoon, T. Li, J. Zhou, H. Hu, M. Abo, K. Iokibe, R. Koga, and Y. Iwasaka, "Ground-based network observation of Asian dust events of April 1998 in East Asia," J. Geophys. Res. **106**, 18 345–18 359 (2001).
9. A. P. Chaikovsky, A. P. Ivanov, Yu. S. Balin, A. V. Elnikov, G. F. Tulinov, I. I. Plusnin, O. A. Bukin, and B. B. Chen, "CIS-LiNet—lidar network for monitoring aerosol and ozone in CIS regions," in *Reviewed and Revised Papers Presented at the 23d ILRC*, Ed. by C. Nagasava and N. Sugimoto (Nara, Japan, 2006), p. 671–672.
10. J. Bosenberg and R. M. Hoff, *Plan for the Implementation of the GAW Aerosol Lidar Observation Network GALION* (WMO, 2007), no. 1443.
11. S. P. Burton, E. Chemyakin, X. Liu, K. Knobelspiesse, S. Stamnes, P. Sawamura, R. H. Moore, C. A. Hostetler, and R. A. Ferrare, "Information content and sensitivity of the $3\beta + 2\alpha$ lidar measurement system for aerosol microphysical retrievals," Atmos. Meas. Tech **9**, 5555–5574 (2016).
12. G. Pappalardo, A. Amodeo, A. Apituley, A. Comeron, V. Freudenthaler, H. Linne, A. Ansmann, J. Bosenberg, G. D' Amico, I. Mattis, L. Mona, U. Wandinger, V. Amiridis, L. Alados-Arboledas, D. Nicolae, and M. Wiegner, "EARLINET: Towards an advanced sustainable European aerosol lidar network," Atmos. Meas. Tech. **7**, 2389–2409 (2014).
13. S. V. Samoilova and Yu. S. Balin, "Reconstruction of the aerosol optical parameters from the data of sensing with a multifrequency raman lidar," Appl. Opt. **47**, 6816–6831 (2008).

14. K. Willeke and K. T. Whitby, "Atmospheric aerosol: Size distribution interpretation," J. Air Poll. Control Assoc. **25**, 529–534 (1975).

15. J. T. Twitty, "The inversion of aureole measurements to derive aerosol size distributions," J. Atmos. Sci. **32**, 584–591 (1975).

16. G. I. Gorchakov, I. A. Gorchakova, E. A. Lykosov, V. G. Tolstobrov, and L. S. Turovtseva, "Determination of the smoke have refractive index and microstructure," Izv. Akad. Nauk SSSR. Fiz. Atmos. Okeana **12** (6), 612–619 (1976).

17. V. V. Veretennikov, I. E. Naats, M. V. Panchenko, and V. Ya. Fadeev, "Determination of the smoke have refractive index and microstructure from polarization characteristics of light scattering," Izv. Akad. Nauk SSSR. Fiz. Atmos. Okeana **14** (12), 1313–1317 (1978).

18. V. V. Veretennikov, V. S. Kozlov, I. E. Naats, and V. Ya. Fadeev, "Optical studies of smoke aerosol: An inversion method and its applications," Opt. Lett. **4**, 411–413 (1979).

19. V. E. Zuev and I. E. Naats, *Inverse Problems of Laser Sounding* (Nauka, Novosibirsk, 1982) [in Russian].

20. R. F. Rakhimov, V. S. Kozlov, M. V. Panchenko, A. G. Tumakov, and V. P. Shmargunov, "Properties of atmospheric aerosol in smoke plumes from forest fires according to spectronephelometer measurements," Atmos. Ocean. Opt. **27** (3), 275–282 (2014).

21. E. V. Makienko, R. F. Rakhimov, Yu. A. Pkhalagov, and V. N. Uzhegov, "Microphysical interpretation of the anomalous spectral behavior of aerosol extinction along a ground path," Atmos. Ocean. Opt. **16** (12), 1008–1012 (2003).

22. V. V. Veretennikov, "Simultaneous determination of aerosol microstructure and refractive index from sun photometry data," Atmos. Ocean. Opt. **20** (3), 192–199 (2007).

23. V. V. Veretennikov, "Retrieval of microstructure parameters of coarse-mode aerosol using their regression relationships with spectral extinction of light in the IR," Atmos. Ocean. Opt. **30** (6), 554–563 (2017).

24. T. V. Bedareva, M. A. Sviridenkov, and T. B. Zhuravleva, "Retrieval of aerosol optical and microphysical characteristics according to data of ground-based spectral measurements of direct and scattered solar radiation. Part 1. Testing of algorithm," Atmos. Ocean. Opt. **26** (1), 24–34 (2013).

25. F. C. Bohren and D. R. Huffman, *Absorption and Scattering of Light by Small Particles* (John Wiley & Sons, Inc, New York, 1983).

26. D. Muller, U. Wandinger, and A. Ansmann, "Microphysical particle parameters from extinction and backscatter lidar data by inversion with regularization: Theory," Appl. Opt. **38**, 2346–2357 (1999).

27. C. Bockmann, "Hybrid regularization method for the ill-posed inversion of multiwavelength lidar data in the retrieval of aerosol size distribution," Appl. Opt. **40**, 1329–1342 (2001).

28. C. Bockmann, I. Mironova, D. Muller, L. Schneidenbach, and R. Nessler, "Microphysical aerosol parameters from multiwavelength lidar," J. Opt. Soc. Am. A **22** (3), 518–528 (2005).

29. I. Veselovskii, A. Kolgotin, V. Griaznov, D. Muller, K. Franke, and D. M. Whiteman, "Inversion of multiwavelength raman lidar data for retrieval of bimodal aerosol size distribution," Appl. Opt. **43**, 1180–1195 (2004).

30. I. Veselovski, A. Kolgotin, D. Muller, and D. M. Whiteman, "Information content of multiwavelength lidar data with respect to microphysical particle properties derived from eigenvalue analysis," Appl. Opt. **44**, 5292–5303 (2005).

31. A. Kolgotin and D. Muller, "Theory of inversion with two-dimensional regularization: Profiles of microphysical particle properties derived from multiwavelength lidar measurements," Appl. Opt. **47**, 4472–4490 (2008).

32. A. H. Omar, D. M. Winker, M. A. Vaughan, Y. Hu, Ch. H. Trepte, R. A. Ferrare, K.-P. Lee, Ch. A. Hostetler, Ch. Kittaka, R. R. Rogers, R. E. Kuehn, and Zh. Lie, "The CALIPSO automated aerosol classification and lidar ratio selection algorithm," J. Atmos. Ocean. Technol **26** (10), 1994–2014 (2009).

33. I. Veselovskii, O. Dubovik, A. Kolgotin, T. Lapyonok, P. Di Girolamo, D. Summa, D. M. Whiteman, M. Mishchenko, and D. Tanre, "Application of randomly oriented spheroids for retrieval of dust particle parameters from multiwavelength lidar measurements," J. Geophys. Res. **115**, D21203 (2010).

34. I. Veselovskii, O. Dubovik, A. Kolgotin, M. Korenskiy, D. N. Whiteman, K. Allakhverdiev, and F. Huseyinoglu, "Linear estimation of particle bulk parameters from multi-wavelength lidar measurements," Atmos. Meas. Tech **5**, 1135–1145 (2012).

35. D. Muller, I. Veselovskii, A. Kolgotin, M. Tesche, A. Ansmann, and O. Dubovik, "Vertical profiles of pure dust and mixed smoke-dust plumes inferred from inversion of multiwavelength raman/polarization lidar data and comparison to AERONET retrievals and in situ observations," Appl. Opt. **52**, 3178–3202 (2013).

36. J. Wagner, A. Ansmann, U. Wandinger, P. Seifert, A. Chwarz, M. Tesche, A. Chaikovsky, and O. Dubovik, "Evaluation of the Lidar/Radiometer Inversion Code (LIRIC) to determinate microphysical properties of volcanic and desert dust," Atmos. Meas. Tech. **6**, 1707–1724 (2013).

37. E. Chemyakin, D. Muller, Sh. Burton, A. Kolgotin, Ch. Hostetler, and R. Ferrare, "Arrange and average algorithm for the retrieval of aerosol parameters from multiwavelength high-spectral-resolution lidar/Raman lidar data," Appl. Opt. **53**, 7252–7266 (2014).

38. E. Chemyakin, S. Burton, A. Kolgotin, D. Muller, C. Hostetler, and R. Ferrare, "Retrieval of aerosol parameters from multiwavelength lidar: Investigation of the underlying inverse mathematical problem," Appl. Opt. **5**, 2188–2202 (2016).

39. M. Kahnert and E. Andersson, "How much information do extinction and backscattering measurements contain about the chemical composition of atmospheric aerosol?," Atmos. Chem. Phys. **17**, 3423–3444 (2017).

40. M. D. Alexandrov and M. I. Mishchenko, "Information content of bistatic lidar observations of aerosols from space," Opt. Express. **25** (4), A134–A150 (2017).

41. M. I. Mishchenko, J. W. Hovenier, and L. D. Travis, *Light Scattering by Nonspherical Particles* (Academic Press, San Diego, CA, USA, 2000).
42. M. I. Mishchenko, L. D. Travis, and A. A. Lacis, *Scattering, Absorption, and Emission of Light by Small Particles* (Cambridge University Press, Cambridge, United Kingdom, 2002).
43. O. Dubovik, A. Sinyuk, T. Lapyonok, B. N. Holben, M. Mishchenko, P. Yang, T. F. Eck, H. Volten, O. Munoz, B. Veihelmann, W. J. van der Zande, J.-F. Leon, M. Sorikin, and I. Slutsker, "Application of spheroid momels to account for aerosol particle nonsphericity in remote sensing of desert dust," J. Geophys. Res. **111**, D11208 (2006).
44. S. V. Samoilova, M. A. Sviridenkov, and I. E. Penner, "Retrieval of the particle size distribution funcion from the data of lidar sensing under the assumption of known refractive index," Appl. Opt. **55**, 8022–8029 (2016).
45. S. V. Samoilova, "Retrieval of complex refractive index from lidar measurements: possibilities and limitations," Opt. Atmos. Okeana **27** (3), 197–206 (2014).
46. S. V. Samoilova, I. E. Penner, G. P. Kokhanenko, and Yu. S. Balin, "Simultaneous reconstruction of two microphysical aerosol characteristics from the lidar data," J. Quant. Spectrosc. Radiat. Transfer **222–223**, 35–44 (2019).
47. Ch. Verhaege, V. Shcherbakov, and P. Personne, "Limitations on retrieval of complex refractive index of spherical particles from scattering measurements," J. Quant. Spectrosc. Radiat. Transfer **109**, 2338–2348 (2008).
48. Ch. Verhaege, V. Shcherbakov, and P. Personne, "Retrieval of complex refractive index and size distribution of spherical particles from dual-polarization polar nephelometer data," J. Quant. Spectrosc. Radiat. Transfer **110**, 1690–1697 (2009). https://doi.org/10.1016/j.jqsrt.2009.01.004
49. A. Lopatin, O. Dubovik, A. Chaikovsky, P. Goloub, T. Lapyonok, D. Tanre, and P. Litvinov, "Enhancement of aerosol characterization using synergy of lidar and sun-photometer coincident observations: The GARRLiC algorithm," Atmos. Meas. Tech. **6**, 2065–2088 (2013).
50. A. Chaikovsky, O. Dubovik, B. Holben, A. Bril, Ph. Goloub, D. Tanre, G. Pappalardo, U. Wandinger, L. Chaikovskaya, S. Denisov, J. Grudo, A. Lopatin, Ya. Karol, T. Lapyonok, V. Amiridis, A. Ansmann, and A. Apituley, L. Allados-Arboledas, I. Binietoglou, A. Boselli, G. D'Amico, V. Freudenthaler, D. Giles, M. J. Granados-Munoz, P. Kokkalis, D. Nicolae, S. Oshchepkov, A. Papayannis, M. R. Perrone, A. Pietruczuk, F. Rocadenbosch, M. Sicard, I. Slutsker, C. Talianu, Tomasi De, Tsekeri F., Wagner A., and X. Wang, "Lidar-Radiometer Inversion Code (LIRIC) for the retrieval of vertical aerosol properties from combined lidar/radiometer data: Development and distribution in EARLINET," Atmos. Meas. Tech. **9**, 1181–1205 (2016). https://doi.org/10.5194/amt-9-1181-2016
51. A. N. Tikhonov and V. Ya. Arsenin, *Methods for Solution of Incorrect Problems* (Nauka, Moscow, 1986) [in Russian].
52. G. I. Vasilenko, *Signal Retrieval Theory* (Sovetskoe radio, Moscow, 1979) [in Russian].
53. S. Samoilova, M. Sviridenkov, I. Penner, G. Kokhanenko, and Yu. Balin, "Retrieval of the tropospheric aerosol microphysical characteristics from the data of multifrequency lidar sensing," EPJ Web Conf. 2018. 28th Laser Radar Conf. **176**. https://doi.org/10.1051/epjconf/201817605055. Cited June 28, 2019).
54. T. V. Bedareva, M. A. Sviridenkov, and T. B. Zhuravleva, "Retrieval of aerosol optical and microphysical characteristics according to data from ground-based spectral measurements of direct and diffuse solar radiation. Part 2. Algorithm testing," Atmos. Ocean. Opt. **26** (2), 107–117 (2013).

Translated by A. Nikol'skii